

Air Force Institute of Technology

AFIT Scholar

Faculty Publications

9-23-2019

Generating Electromagnetic Schell-Model Sources Using Complex Screens with Spatially Varying Auto- and Cross-Correlation Functions

Milo W. Hyde IV

Air Force Institute of Technology

Follow this and additional works at: <https://scholar.afit.edu/facpub>

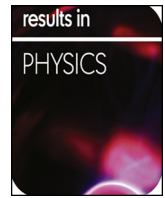


Part of the [Applied Statistics Commons](#), and the [Optics Commons](#)

Recommended Citation

Hyde, M. W. (2019). Generating electromagnetic Schell-model sources using complex screens with spatially varying auto- and cross-correlation functions. *Results in Physics*, 15, 102663. <https://doi.org/10.1016/j.rinp.2019.102663>

This Article is brought to you for free and open access by AFIT Scholar. It has been accepted for inclusion in Faculty Publications by an authorized administrator of AFIT Scholar. For more information, please contact richard.mansfield@afit.edu.



Generating electromagnetic Schell-model sources using complex screens with spatially varying auto- and cross-correlation functions[☆]

Milo W. Hyde IV

Air Force Institute of Technology, Dayton, OH 45433, USA

ARTICLE INFO

Keywords:

Beam shaping
Coherence
Polarization
Random sources
Schell-model sources
Statistical optics

ABSTRACT

We present a method to generate any physically realizable electromagnetic Schell-model source. Our technique can be directly implemented on existing vector-beam generators that utilize spatial light modulators for coherence control, beam shaping, and relative phasing. This work significantly extends published research on the subject, where control over the partially coherent source's cross-spectral density matrix was limited.

We begin by presenting the statistical optics theory necessary to derive and implement our method. We then apply our technique, both analytically and in simulation, to produce two electromagnetic Schell-model sources from the literature. We demonstrate control over the full cross-spectral density matrices of both partially coherent beams. We compare the simulated results of these two sources to the corresponding theoretical or designed quantities to validate our approach. We find, through examination of the two-dimensional correlation coefficients, that both sources converge to their desired, ensemble (or by ergodicity, “long-time”) statistics within 500 random field instances.

Our method and subsequent findings will be useful in any application where control over beam shape, polarization, and spatial coherence are important. These include but are not limited to free-space/underwater optical communications, directed energy, medicine, atomic optics, and optical tweezers.

Introduction

Since Emil Wolf's seminal work on coherence and polarization in the early 2000s [1,2], many different vector or electromagnetic Schell-model sources have been developed. These beams have been designed to have dynamic polarization, coherence, and beam-shape characteristics for applications from directed energy and free-space optical communications to atomic optics and optical tweezers [3–14].

Subsequently, techniques to physically realize these sources have been developed [3–6,15–26]. The most common approach uses spatial light modulators (SLMs) in a Mach-Zehnder-interferometer-like setup [3,17–19,22,25,26]. Light from a common source (typically, a laser) is polarization split into two orthogonal child beams. An SLM or SLMs placed along the interferometer optical paths control the beam shape, coherence, and relative phasing of the child beams. The beams are then recombined to form a stochastic realization of the desired vector Schell-model source (VSMS). This stochastic field realization is spatially coherent. Partial coherence is produced by cycling the SLM commands at a high rate.

Several recent papers have presented theory and some experimental

results where complex VSMSs have been produced using the above approach [3,17–20,25,22,26–28]. A key theoretical problem present in the cited works has been control over the spatial cross-correlation function of the orthogonal child beams. As will be shown, the cross-correlation function of the child beams is predominately determined by their individual self- or auto-correlation functions. Mathematically, this affects the off-diagonal elements of the cross-spectral density (CSD) matrix and physically limits the ability to synthesize VSMSs with S_2 and S_3 Stokes vector components [29].

For instances, Refs. [3,18,25–27] discuss synthesizing electromagnetic Gaussian Schell-model sources (EGSMSs). The EGSM parameter constraints derived therein are much more restrictive than the physical source realizability conditions derived in Refs. [3,30]. More extreme examples can be found in Refs. [22,28]. In the former, the authors find only one condition under which an electromagnetic multi-Gaussian Schell-model source (EMGSM) can be produced with off-diagonal CSD matrix elements [22]. In the latter, the inability to control the full CSD matrix limits far-zone beam control to only two Poincaré sphere parameters—the total intensity S_0 and the degree of polarization \mathcal{P} , S_0 and the angle of polarization ψ , or S_0 and the ellipticity angle χ

[☆] The views expressed in this paper are those of the authors and do not reflect the official policy or position of the U.S. Air Force, the Department of Defense, or the U.S. Government.

E-mail address: milo.hyde@us.af.mil.

<https://doi.org/10.1016/j.rinp.2019.102663>

Received 27 June 2019; Accepted 12 September 2019

Available online 23 September 2019

2211-3797/ Published by Elsevier B.V. This is an open access article under the CC BY license (<http://creativecommons.org/licenses/by/4.0/>).

[28].

In this paper, we present a way to control the full CSD matrix and therefore produce any physically realizable VSMS. Our method does not require any additional optical components or hardware and can be directly implemented using the interferometer setup highlighted above and the more detailed setups described in Refs. [3,18,22].

We begin by presenting the theory underpinning our approach. Then, as examples, we generalize the work presented in Refs. [22,28], namely, to produce any physically realizable EMGSMS and an engineered VSMS that radiates a beam with a customizable far-zone polarization state, i.e., controllable S_0 , \mathcal{P} , ψ , and χ .

We demonstrate and validate our approach with Monte Carlo simulations, where we generate an EMGSMS which, until now, has been impossible to produce, and an engineered VSMS that radiates a far-zone beam with an S_0 , \mathcal{P} , ψ , and χ that are complex grayscale images. We compare the simulated results to the EMGSMS theoretical predictions or the desired S_0 , \mathcal{P} , ψ , and χ images, whichever is applicable. We present the correlation coefficients versus Monte Carlo trial number to show the convergence of our method. The correlation coefficient results will be useful to those who implement our technique for a specific application. Lastly, we conclude this paper with a summary of our analysis and a brief list of potential applications.

Theory

The statistical behavior of a wide-sense stationary (WSS), planar, partially coherent source is fully described by its CSD matrix [2,31], viz.,

$$\mathbf{W}(\rho_1, \rho_2, \omega) = \begin{bmatrix} W_{xx}(\rho_1, \rho_2, \omega) & W_{xy}(\rho_1, \rho_2, \omega) \\ W_{yx}(\rho_1, \rho_2, \omega) & W_{yy}(\rho_1, \rho_2, \omega) \end{bmatrix}, \quad (1)$$

where ω is the radian frequency (hereafter assumed and suppressed), $\rho_{1,2} = \hat{x}x_{1,2} + \hat{y}y_{1,2}$, $W_{\alpha\beta}(\rho_1, \rho_2) = \langle E_\alpha(\rho_1)E_\beta^*(\rho_2) \rangle$, and $\alpha, \beta = x, y$. E_α is the stochastic complex amplitude of the optical field's α polarization component.

Here, we assume that \mathbf{W} takes a Schell-model form [2,31], such that

$$W_{\alpha\beta}(\rho_1, \rho_2) = \tau_\alpha(\rho_1)\tau_\beta^*(\rho_2)\mu_{\alpha\beta}(\rho_1 - \rho_2), \quad (2)$$

where τ_α is the deterministic complex amplitude of the α field component and $\mu_{\alpha\beta}$ is the complex cross-correlation function of the α and β field components.

When it comes to physically realizing a particular \mathbf{W} , controlling $\mu_{\alpha\beta}$, where $\alpha \neq \beta$ (in more direct terms, μ_{xy}), has been a challenge. Overcoming this challenge is the purpose of this paper. In the sections that follow, we show that μ_{xy} can be controlled by spatially varying the cross-correlation coefficient between the white-noise, Gaussian random numbers that seed E_x and E_y .

Generating stochastic vector field realizations

We begin with the following model for a stochastic vector field realization:

$$\mathbf{E}(\rho) = \hat{x}\tau_x(\rho)T_x(\rho) + \hat{y}\tau_y(\rho)T_y(\rho), \quad (3)$$

where T_α is a random complex "screen" (for the α field component) formed from circular complex Gaussian random numbers. Taking the vector auto-correlation of Eq. (3), i.e.,

$$\langle E_\alpha(\rho_1)E_\beta^*(\rho_2) \rangle = \tau_\alpha(\rho_1)\tau_\beta^*(\rho_2)\langle T_\alpha(\rho_1)T_\beta^*(\rho_2) \rangle, \quad (4)$$

and comparing the result to Eq. (2) yields the equality

$$\mu_{\alpha\beta}(\rho_1 - \rho_2) = \langle T_\alpha(\rho_1)T_\beta^*(\rho_2) \rangle. \quad (5)$$

Thus, a field instance drawn from the WSS process described by \mathbf{W} can be generated by producing two correlated complex screens, T_x and T_y , with correlation functions given by $\mu_{\alpha\beta}$. The challenge of course, is

generating T_x and T_y when, in general, $\mu_{xx} \neq \mu_{yy} \neq \mu_{xy}$.

We start with $\alpha = \beta$, as this does affect the $\alpha \neq \beta$ case. The $\alpha = \beta$ case concerns the diagonal elements of \mathbf{W} . Since \mathbf{W} is of Schell-model form, we can generate instances of T_x and T_y with the desired μ_{xx} and μ_{yy} , respectively, by filtering delta-correlated circular complex Gaussian random numbers. For computational efficiency, the filtering operation is commonly performed in the spatial frequency domain via the convolution theorem and the fast Fourier transform (FFT). This process has been derived in the literature many times [18,22,32–36]. The final result is

$$T_\alpha[i, j] = \sum_{m, n} r_\alpha[m, n] \sqrt{\frac{\Phi_{\alpha\alpha}[m, n]}{2L_x L_y}} \exp\left(j\frac{2\pi}{N_x}im\right) \exp\left(j\frac{2\pi}{N_y}jn\right), \quad (6)$$

where r_α is an $N_y \times N_x$ grid of zero-mean, unit-variance circular complex Gaussian random numbers, i, j are discrete spatial indices, m, n are discrete spatial frequency indices, and L_x, L_y are the grid dimensions in meters in the x and y directions, respectively. Lastly, $\Phi_{\alpha\alpha}$ is the spatial power spectrum of T_α , i.e.,

$$\Phi_{\alpha\alpha}(\mathbf{f}) = \int \int_{-\infty}^{\infty} \mu_{\alpha\alpha}(\rho) \exp(-j2\pi\mathbf{f}\cdot\rho) d^2\rho, \quad (7)$$

where $\mathbf{f} = \hat{x}f_x + \hat{y}f_y$, via the Wiener-Khinchin theorem [31,37].

Moving on to the $\alpha \neq \beta$ case, evaluating Eq. (6) creates a T_α with the desired ensemble auto-correlation $\mu_{\alpha\alpha}$. For μ_{xy} , we need to examine the cross-correlation of T_x with T_y , namely,

$$\begin{aligned} \langle T_x[i_1, j_1]T_y^*[i_2, j_2] \rangle &= \sum_{m_1, n_1} \sum_{m_2, n_2} \langle r_x[m_1, n_1]r_y^*[m_2, n_2] \rangle \\ &\times \frac{\sqrt{\Phi_{xx}[m_1, n_1]\Phi_{yy}[m_2, n_2]}}{2L_x L_y} \exp\left[j\frac{2\pi}{N_x}(i_1 m_1 - i_2 m_2)\right] \\ &\times \exp\left[j\frac{2\pi}{N_y}(j_1 n_1 - j_2 n_2)\right] \end{aligned} \quad (8)$$

Recalling Eqs. (4) and (5), clearly, μ_{xy} (and subsequently, \mathbf{W} 's off-diagonal elements) depend on the diagonal elements of \mathbf{W} via Φ_{xx} and Φ_{yy} . The moment $\langle r_x[m_1, n_1]r_y^*[m_2, n_2] \rangle$ determines the degree of control over μ_{xy} .

In past works,

$$\langle r_x[m_1, n_1]r_y^*[m_2, n_2] \rangle = 2R\delta[m_1 - m_2]\delta[n_1 - n_2], \quad (9)$$

where $\delta[x]$ is the discrete Dirac delta function and R is the correlation coefficient between the r_x and r_y random numbers [3,18,22,25–28]. Simplifying Eq. (8) with this result produces

$$\begin{aligned} \langle T_x[i_1, j_1]T_y^*[i_2, j_2] \rangle &= \sum_{m, n} R\sqrt{\Phi_{xx}[m, n]\Phi_{yy}[m, n]} \\ &\times \exp\left[j\frac{2\pi}{N_x}m(i_1 - i_2)\right] \exp\left[j\frac{2\pi}{N_y}n(j_1 - j_2)\right] \frac{1}{L_x L_y} \end{aligned} \quad (10)$$

Thus, to control μ_{xy} ,

$$R\sqrt{\Phi_{xx}[m, n]\Phi_{yy}[m, n]} = \Phi_{xy}[m, n], \quad (11)$$

where Φ_{xy} is the cross-power spectrum and equal to the Fourier transform of μ_{xy} [see Eq. (7)]. With R being constant, there is little flexibility in controlling μ_{xy} . We present an example of this later on in the paper. Next, however, we allow R to spatially vary and discuss how to generate r_x and r_y (ultimately, T_x , T_y , and \mathbf{E}) with a spatially varying R .

Spatially varying R

Returning briefly to Eq. (8), we expand the moment $\langle r_x[m_1, n_1]r_y^*[m_2, n_2] \rangle$ in terms of the real and imaginary parts of r_x and r_y , namely,

$$\begin{aligned} \langle r_x[m_1, n_1]r_y^*[m_2, n_2] \rangle &= \langle r_x^r[m_1, n_1]r_y^r[m_2, n_2] \rangle + \langle r_x^i[m_1, n_1]r_y^i[m_2, n_2] \rangle \\ &+ j(\langle r_x^i[m_1, n_1]r_y^r[m_2, n_2] \rangle - \langle r_x^r[m_1, n_1]r_y^i[m_2, n_2] \rangle), \end{aligned} \quad (12)$$

where the superscripts “r” and “i” refer to the real and imaginary parts, respectively. The moments in Eq. (12) must be

$$\begin{aligned} & \langle r_x^r[m_1, n_1] r_y^r[m_2, n_2] \rangle + \langle r_x^i[m_1, n_1] r_y^i[m_2, n_2] \rangle \\ & = 2R^r[m_1, n_1] \delta[m_1 - m_2] \delta[n_1 - n_2] \\ & \langle r_x^i[m_1, n_1] r_y^r[m_2, n_2] \rangle - \langle r_x^r[m_1, n_1] r_y^i[m_2, n_2] \rangle \\ & = 2R^i[m_1, n_1] \delta[m_1 - m_2] \delta[n_1 - n_2] \end{aligned} \quad (13)$$

to ensure that the generated source \mathbf{W} is of Schell-model form—more accurately, that T_x and T_y are jointly homogeneous or equivalently that $\langle T_x[i_1, j_1] T_y^*[i_2, j_2] \rangle$ is a function of only $i_1 - i_2, j_1 - j_2$ [37]. Substituting the above into Eq. (8) and simplifying yields

$$\begin{aligned} \langle T_x[i_1, j_1] T_y^*[i_2, j_2] \rangle & = \sum_{m,n} (R^r[m, n] + jR^i[m, n]) \sqrt{\Phi_{xx}[m, n] \Phi_{yy}[m, n]} \\ & \times \exp\left[j \frac{2\pi}{N_x} m(i_1 - i_2)\right] \exp\left[j \frac{2\pi}{N_y} n(j_1 - j_2)\right] \frac{1}{L_x L_y}. \end{aligned} \quad (14)$$

This last relation leads to an expression similar to Eq. (11), but much more general:

$$R^{r,i}[m, n] = \frac{\Phi_{xy}^{r,i}[m, n]}{\sqrt{\Phi_{xx}[m, n] \Phi_{yy}[m, n]}}, \quad (15)$$

where $R^{r,i} \in [-1, 1]$.

The next step is to generate r_x and r_y with cross-correlation coefficients $R^{r,i}$ given in Eq. (15). This can be achieved using Cholesky decomposition [22,38,39]. We note that using Cholesky decomposition to generate r_x and r_y for a general source given by the covariance matrix in Eq. (12) is impractical for reasonably sized grids. For example, assume that the desired T_x and T_y are 512×512 grids, which is a common size for commercially available SLMs. The covariance matrix, in this case, is a staggering $2^{20} \times 2^{20}$ matrix, which requires a supercomputer to store and compute the Cholesky factors.

Fortunately, there is a much more efficient way to generate r_x and r_y , since T_x and T_y are jointly homogeneous. Note that in Eq. (13), the Dirac delta functions reduce the dimensions of the cross-correlation function from four to two. Thus, for any $m_1 = m_2 = m, n_1 = n_2 = n$, the covariance matrix is

$$\begin{aligned} \Sigma & = \begin{bmatrix} \langle r_x^r r_x^r \rangle & \langle r_x^r r_x^i \rangle & \langle r_x^r r_y^r \rangle & \langle r_x^r r_y^i \rangle \\ \langle r_x^i r_x^r \rangle & \langle r_x^i r_x^i \rangle & \langle r_x^i r_y^r \rangle & \langle r_x^i r_y^i \rangle \\ \langle r_y^r r_x^r \rangle & \langle r_y^r r_x^i \rangle & \langle r_y^r r_y^r \rangle & \langle r_y^r r_y^i \rangle \\ \langle r_y^i r_x^r \rangle & \langle r_y^i r_x^i \rangle & \langle r_y^i r_y^r \rangle & \langle r_y^i r_y^i \rangle \end{bmatrix} \\ & = \begin{bmatrix} 1 & 0 & R^r & -R^i \\ 0 & 1 & R^i & R^r \\ R^r & R^i & 1 & 0 \\ -R^i & R^r & 0 & 1 \end{bmatrix} \end{aligned} \quad (16)$$

where evaluation of $r_x^r, r_x^i, r_y^r, r_y^i, R^r$, and R^i at a particular m, n is implied. Calculating the Cholesky factors for Σ is a relatively straightforward task, i.e.,

$$\begin{aligned} \Sigma & = \mathbf{L}\mathbf{L}^T \\ \mathbf{L} & = \begin{bmatrix} 1 & 0 & 0 & 0 \\ 0 & 1 & 0 & 0 \\ R^r & R^i & \sqrt{1 - (R^r)^2 - (R^i)^2} & 0 \\ -R^i & R^r & 0 & \sqrt{1 - (R^r)^2 - (R^i)^2} \end{bmatrix}. \end{aligned} \quad (17)$$

We can now generate r_x and r_y by first producing four $N_y \times N_x$ grids of zero-mean, unit-variance, independent Gaussian random numbers— r_1, r_2, r_3 , and r_4 in the analysis to follow. Then, using \mathbf{L} , r_x and r_y are

Table 1
Simulated EMGMS Parameters.

A_x	1.5
A_y	1
σ_x	0.5 mm
σ_y	0.8 mm
B_{xy}	$0.5 \exp(-j\pi/6)$
δ_{xx}	0.6 mm
δ_{yy}	0.4 mm
δ_{xy}	0.6464 mm
M	40

$$\begin{aligned} r_x[m, n] & = r_1[m, n] + jr_2[m, n] \\ r_y[m, n] & = (r_1[m, n] + jr_2[m, n])(R^r[m, n] - jR^i[m, n]) \\ & + (r_3[m, n] + jr_4[m, n])\sqrt{1 - (R^r[m, n])^2 - (R^i[m, n])^2}. \end{aligned} \quad (18)$$

Lastly, realizations of T_x, T_y , and E can be produced using Eqs. (6) and (3), respectively.

In the next section, we present examples showing how to apply the above analysis to generate any physically realizable EMGMS and an engineered VSMS that radiates a far-zone beam with controllable S_0, \mathcal{P}, ψ , and χ (hereafter referred to as the engineered VSMS).

Examples

EMGMS

The CSD matrix elements of an EMGMS are [3,7]

$$\begin{aligned} W_{\alpha\beta}(\rho_1, \rho_2) & = A_\alpha \exp\left(-\frac{\rho_1^2}{4\sigma_\alpha^2}\right) A_\beta \exp\left(-\frac{\rho_2^2}{4\sigma_\beta^2}\right) \\ & \times B_{\alpha\beta} \frac{1}{C_0} \sum_{m=1}^M \binom{M}{m} \frac{(-1)^{m-1}}{m} \exp\left(-\frac{|\rho_1 - \rho_2|^2}{2m\delta_{\alpha\beta}^2}\right), \end{aligned} \quad (19)$$

where A_α and σ_α are the amplitude and r.m.s width of the α field component, $\delta_{\alpha\beta}$ is the cross-correlation width, $B_{\alpha\beta}$ is the complex cross-correlation coefficient, and C_0 is a normalization factor equal to

$$C_0 = \sum_{m=1}^M \binom{M}{m} \frac{(-1)^{m-1}}{m}. \quad (20)$$

For the above source to be physically realizable, the EMGMS parameters must satisfy [3,7]

$$\begin{aligned} B_{xx} = B_{yy} = 1, \quad |B_{xy}| \leq 1, \quad B_{yx} = B_{xy}^*, \quad \delta_{xy} = \delta_{yx}, \\ \max\{\delta_{xx}, \delta_{yy}\} \leq \delta_{xy} \leq \sqrt{\frac{\delta_{xx}\delta_{yy}}{|B_{xy}|}}. \end{aligned} \quad (21)$$

We note that when $M = 1$, the EMGMS simplifies to an EGMS, and thus, this example includes EGMSs as a special case.

Comparing Eq. (4) to Eq. (19), we see that

$$\tau_\alpha(\rho) = C_\alpha \exp\left(-\frac{\rho^2}{4\sigma_\alpha^2}\right), \quad (22)$$

where C_α is a complex constant, such that $|C_\alpha| = A_\alpha$. When $\alpha = \beta$,

$$\left\langle T_\alpha(\rho_1) T_\alpha^*(\rho_2) \right\rangle = \frac{1}{C_0} \sum_{m=1}^M \binom{M}{m} \frac{(-1)^{m-1}}{m} \exp\left(-\frac{|\rho_1 - \rho_2|^2}{2m\delta_{\alpha\alpha}^2}\right). \quad (23)$$

When $\alpha \neq \beta$, we find that

$$\begin{aligned} \arg(C_\alpha C_\beta^*) & = \arg(B_{xy}) \\ \langle T_x(\rho_1) T_y^*(\rho_2) \rangle & = |B_{xy}| \frac{1}{C_0} \sum_{m=1}^M \binom{M}{m} \frac{(-1)^{m-1}}{m} \exp\left(-\frac{|\rho_1 - \rho_2|^2}{2m\delta_{xy}^2}\right). \end{aligned} \quad (24)$$

We can now apply the analysis in Sections “Generating stochastic vector field realizations” and “Spatially varying R ” to generate EMGMS field instances. Using Eq. (7), the spatial power spectrum $\Phi_{\alpha\alpha}$

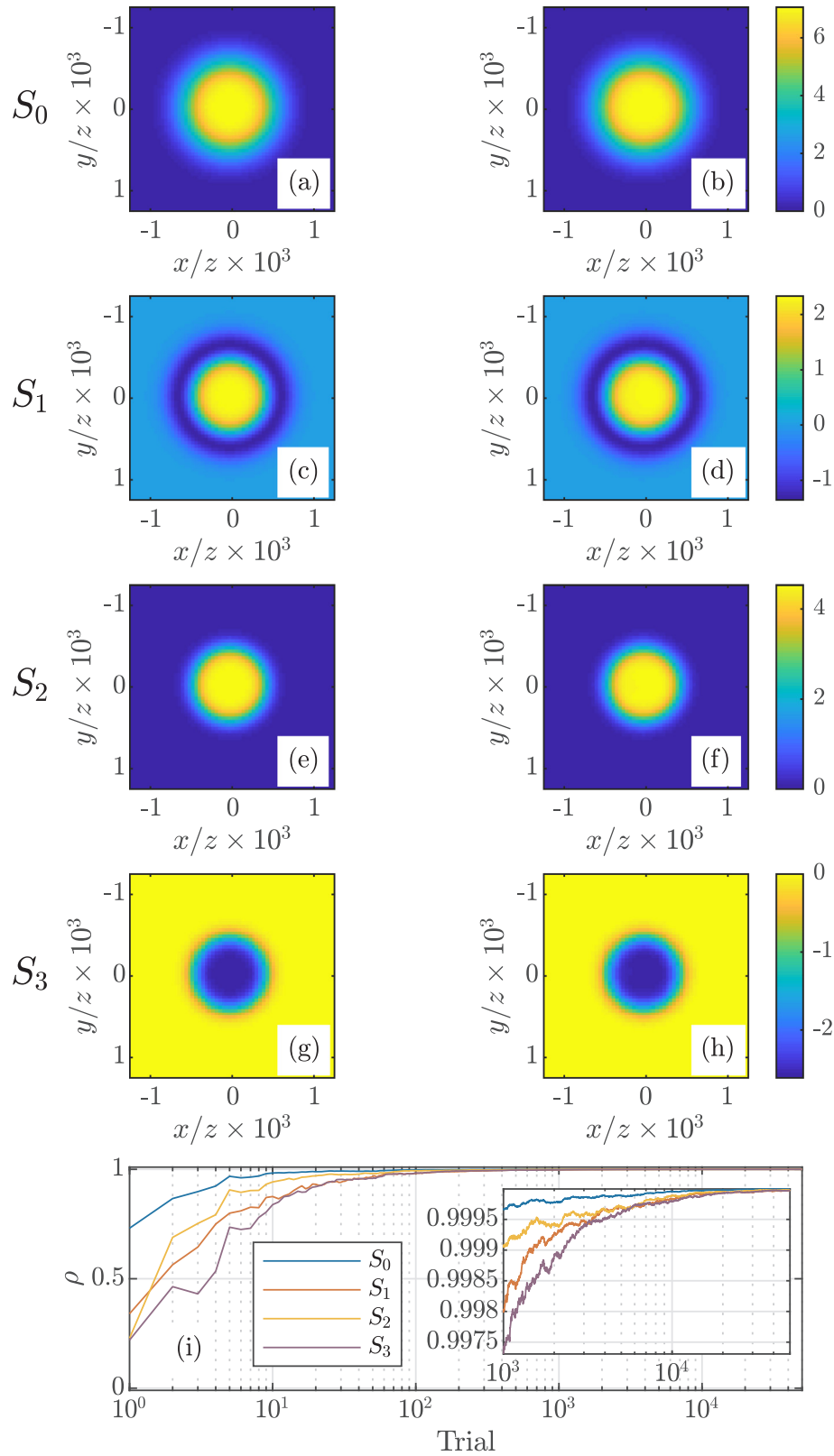


Fig. 1. Theoretical (left column) and simulated (right column) EMGSMS Stokes vector results—(a) S_0^{thy} , (b) S_0^{sim} , (c) S_1^{thy} , (d) S_1^{sim} , (e) S_2^{thy} , (f) S_2^{sim} , (g) S_3^{thy} , (h) S_3^{sim} , and (i) two-dimensional correlation coefficients C of the simulated Stokes parameters versus trial number. The inset in (i) shows C from trials 1000–50,000.

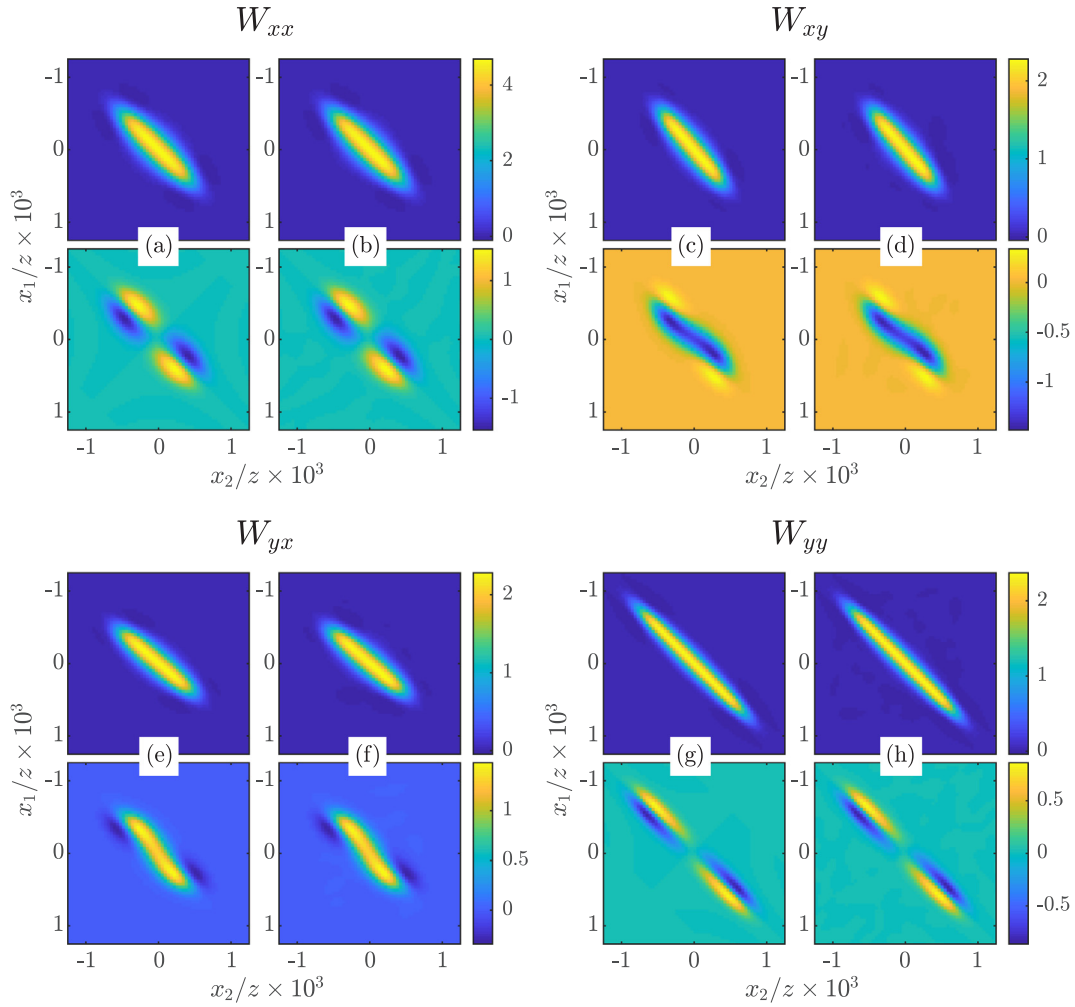


Fig. 2. EMGSMS $\mathbf{W}(x_1, 0, x_2, 0)$ results—(a) real (top) and imaginary (bottom) parts of W_{xx}^{thy} , (b) real (top) and imaginary (bottom) parts of W_{xx}^{sim} , (c) real (top) and imaginary (bottom) parts of W_{xy}^{thy} , (d) real (top) and imaginary (bottom) parts of W_{xy}^{sim} , (e) real (top) and imaginary (bottom) parts of W_{yx}^{thy} , (f) real (top) and imaginary (bottom) parts of W_{yx}^{sim} , (g) real (top) and imaginary (bottom) parts of W_{yy}^{thy} , and (h) real (top) and imaginary (bottom) parts of W_{yy}^{sim} .

is

$$\begin{aligned} \Phi_{\alpha\alpha}(f) &= \frac{2\pi\delta_{\alpha\alpha}^2}{C_0} \sum_{m=1}^M \binom{M}{m} (-1)^{m-1} \exp(-2\pi^2 m \delta_{\alpha\alpha}^2 f^2) \\ &= \frac{2\pi\delta_{\alpha\alpha}^2}{C_0} \{1 - [1 - \exp(-2\pi^2 \delta_{\alpha\alpha}^2 f^2)]\}^M. \end{aligned} \quad (25)$$

We now find the required $R^{r,i}$ using Eq. (15):

$$\begin{aligned} R^i[m, n] &= 0 \\ R^r[m, n] &= \frac{|B_{xy}| \delta_{xy}^2}{\delta_{xx} \delta_{yy}} \{1 - [1 - \exp(-2\pi^2 \delta_{xy}^2 f^2)]\}^M \\ &\quad \times \prod_{\alpha=x,y} \{1 - [1 - \exp(-2\pi^2 \delta_{\alpha\alpha}^2 f^2)]\}^{-1/2}, \end{aligned} \quad (26)$$

where $f = \sqrt{(m/L_x)^2 + (n/L_y)^2}$ is the discrete spatial frequency. With $R^{r,i}$, we use Eq. (18) to find r_x, r_y , Eq. (6) to generate T_x, T_y , and lastly, Eq. (3) to form an EMGSMS field instance.

It is important and insightful to check if $R^{r,i} \in [-1, 1]$. Clearly, R^i satisfies this condition. For R^r , we recall the realizability criteria given in Eq. (21), and for convenience, let $R^r = ag(f)$, where

$$\begin{aligned} a &= \delta_{xy}^2 \frac{|B_{xy}|}{\delta_{xx} \delta_{yy}} \\ g(f) &= \frac{1 - [1 - \exp(-2\pi^2 \delta_{xy}^2 f^2)]^M}{\prod_{\alpha=x,y} \{1 - [1 - \exp(-2\pi^2 \delta_{\alpha\alpha}^2 f^2)]\}^{1/2}}. \end{aligned} \quad (27)$$

Considering the fork inequality on the second line of Eq. (21), $0 \leq a \leq 1$, where $a = 0$ when $B_{xy} = 0$ and $a = 1$ when δ_{xy} equals its maximum physically allowed value. For g , even if δ_{xy} equals its minimum value, the numerator of g is a faster (narrower) function of f than the denominator, and therefore, $0 \leq g(f) \leq 1$ for all f . The above conditions on a and g imply that $0 \leq R^r \leq 1$. Most importantly, since all δ_{xy} satisfying the fork inequality in Eq. (21) map to an $R^{r,i} \in [-1, 1]$, all physically realizable EMGSMSs can be generated using the procedure and analysis presented in the previous paragraph.

To demonstrate the significance of this contribution, we briefly discuss generating EMGSMSs using the approach in Refs. [3,25,22,18,26–28]. As discussed in Section “Generating stochastic vector field realizations”, in past works, Eq. (11) was used to determine a spatially invariant (or constant) R to control μ_{xy} . Reference [22] considered an EMGSMS and derived the following condition:

$$\begin{aligned} \delta_{xx} \delta_{yy} R \prod_{\alpha=x,y} \{1 - [1 - \exp(-2\pi^2 \delta_{\alpha\alpha}^2 f^2)]\}^{1/2} \\ = |B_{xy}| \delta_{xy}^2 \{1 - [1 - \exp(-2\pi^2 \delta_{xy}^2 f^2)]\}^M, \end{aligned} \quad (28)$$

which must hold for all f and is satisfied in only two cases. Letting $R = |B_{xy}|$,

1. If $B_{xy} = 0$, \mathbf{W} is diagonal.
2. If $|B_{xy}| \neq 0$, \mathbf{W} is full and $\delta_{xx} = \delta_{yy} = \delta_{xy}$.

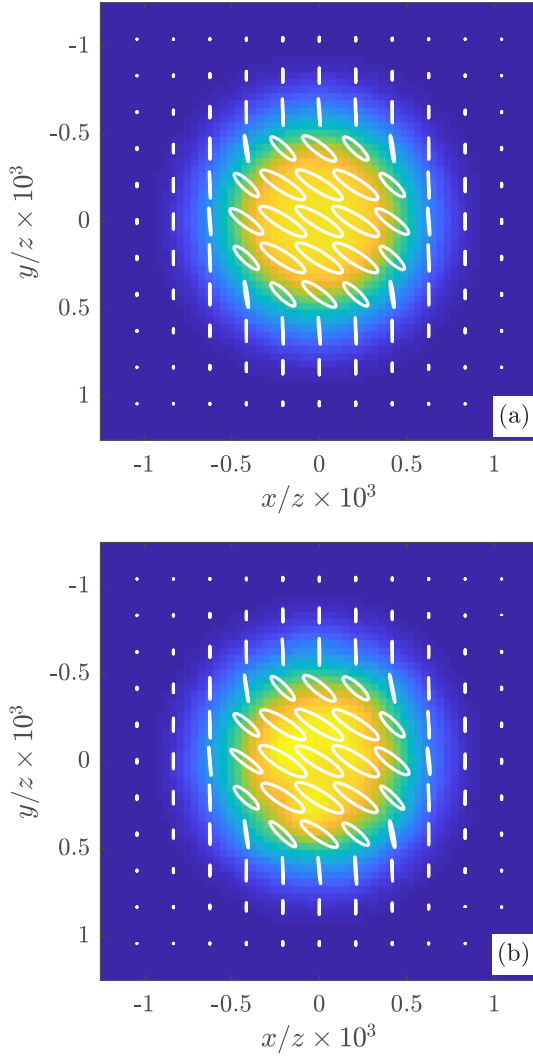


Fig. 3. Polarization ellipses across the beam's profile—(a) theory and (b) simulation (results after 500 trials).

Thus, this prior method can only produce a small subset of physically realizable EMGSMs. This stands in sharp contrast to the technique developed in this paper.

Engineered VSMS

Here, we design an electromagnetic Schell-model source that radiates a far-zone beam with completely controllable Poincaré sphere parameters— S_0 , \mathcal{P} , ψ , and χ . This extends the work in Ref. [28], where using Eq. (11), only two of the parameters could be controlled simultaneously.

We begin with the random optical field given in Eq. (3). Like in Ref. [28], we assume that $\tau_x = \tau_y = \tau$ and that \mathbf{E} is a realization of an electromagnetic quasi-homogeneous source [3,40].

Following the procedure in Ref. [28], we take the vector auto-correlation of Eq. (3), propagate the resulting \mathbf{W} to the far-zone, and then evaluate the far-zone $\underline{\mathbf{W}}$ at $\rho_1 = \rho_2 = \rho$ producing

$$W_{\alpha\beta}(\rho, \rho, z) \approx \frac{\mathcal{F}(0)}{(\lambda z)^2} \Phi_{\alpha\beta}\left(\frac{\rho}{\lambda z}\right), \quad (29)$$

where λ is the wavelength, z is the distance to the far-zone observation point, $\Phi_{\alpha\beta}$ is the auto- or cross-power spectrum [recall Eq. (7)], and \mathcal{F} is the auto-correlation of τ .

The Stokes parameters in terms of the CSD matrix elements are

$$\begin{aligned} S_0 &= W_{xx} + W_{yy} \\ S_1 &= W_{xx} - W_{yy} = S_0 \mathcal{P} \cos(2\psi) \cos(2\chi) \\ S_2 &= W_{xy} + W_{yx} = S_0 \mathcal{P} \sin(2\psi) \cos(2\chi) \\ S_3 &= j(W_{yx} - W_{xy}) = S_0 \mathcal{P} \sin(2\chi), \end{aligned} \quad (30)$$

where S_0 is the total average intensity, $0 \leq \mathcal{P} \leq 1$ is the degree of polarization, $-\pi/2 < \psi \leq \pi/2$ is the angle of polarization, and $-\pi/4 \leq \chi \leq \pi/4$ is the ellipticity angle [2,3,29]. The functional dependencies of the Stokes parameters, Poincaré sphere parameters, and CSD matrix elements on ρ and z are assumed and suppressed. Substituting in Eq. (29) and simplifying produces

$$\begin{aligned} S_0 &= \hat{\Phi}_{xx} + \hat{\Phi}_{yy} \\ S_1 &= \hat{\Phi}_{xx} - \hat{\Phi}_{yy} = S_0 \mathcal{P} \cos(2\psi) \cos(2\chi) \\ S_2 &= 2\text{Re}(\hat{\Phi}_{xy}) = S_0 \mathcal{P} \sin(2\psi) \cos(2\chi) \\ S_3 &= 2\text{Im}(\hat{\Phi}_{xy}) = S_0 \mathcal{P} \sin(2\chi), \end{aligned} \quad (31)$$

where $\hat{\Phi}_{\alpha\beta} = \Phi_{\alpha\beta} \mathcal{F}(0)/(\lambda z)^2$.

We know from Eq. (15) that $\hat{\Phi}_{xy}^{r,i} = R^{r,i} \sqrt{\hat{\Phi}_{xx} \hat{\Phi}_{yy}}$, such that

$$\begin{aligned} \hat{\Phi}_{xx} + \hat{\Phi}_{yy} &= S_0 \\ \hat{\Phi}_{xx} - \hat{\Phi}_{yy} &= S_0 \mathcal{P} \cos(2\psi) \cos(2\chi) \\ 2R^r \sqrt{\hat{\Phi}_{xx} \hat{\Phi}_{yy}} &= S_0 \mathcal{P} \sin(2\psi) \cos(2\chi) \\ 2R^i \sqrt{\hat{\Phi}_{xx} \hat{\Phi}_{yy}} &= S_0 \mathcal{P} \sin(2\chi). \end{aligned} \quad (32)$$

We can now solve these equations for $\hat{\Phi}_{xx}$, $\hat{\Phi}_{yy}$, R^r , and R^i in terms of the Poincaré sphere parameters to yield the desired result:

$$\begin{aligned} \hat{\Phi}_{xx} &= \frac{1}{2} S_0 [1 + \mathcal{P} \cos(2\chi) \cos(2\psi)] \\ \hat{\Phi}_{yy} &= \frac{1}{2} S_0 [1 - \mathcal{P} \cos(2\chi) \cos(2\psi)] \\ R^r &= \frac{\mathcal{P} \cos(2\chi) \sin(2\psi)}{\sqrt{1 - \mathcal{P}^2 \cos^2(2\chi) \cos^2(2\psi)}} \\ R^i &= \frac{\mathcal{P} \sin(2\chi)}{\sqrt{1 - \mathcal{P}^2 \cos^2(2\chi) \cos^2(2\psi)}}. \end{aligned} \quad (33)$$

With Eq. (33), we use Eq. (18) to find r_x , r_y , Eq. (6) to generate T_x , T_y , and lastly, Eq. (3) to form a vector field realization. To observe the desired Poincaré sphere parameters, we must propagate many vector field instances to the far zone and compute the Stokes parameters averaged over the ensemble of random field realizations [see Eq. (30)]. From these Stokes parameters, we then compute S_0 , \mathcal{P} , ψ , and χ .

It is instructive to explore some special polarization cases. We start with unpolarized light, where $\mathcal{P} = 0$. We see at once from Eq. (33) that $\hat{\Phi}_{xx} = \hat{\Phi}_{yy} = S_0/2$ and $R^r = R^i = 0$. These values make physical sense considering that for unpolarized light, the field's vector components, E_x and E_y , have equal average powers ($\hat{\Phi}_{xx} = \hat{\Phi}_{yy}$) and are statistically uncorrelated ($R = 0$).

Proceeding to circular polarization ($\mathcal{P} = 1$ and $\chi = \pi/4, -\pi/4$), we see again that $\hat{\Phi}_{xx} = \hat{\Phi}_{yy} = S_0/2$, but this time $R^r = 0$ and $R^i = 1, -1$ depending on whether the polarization ellipse rotates to the right or to the left. Again, these values are intuitive. Like unpolarized light, circularly polarized light requires E_x and E_y to have equal powers. In addition, it requires that E_x and E_y be perfectly correlated ($|R| = 1$), and E_x to lead or lag E_y in phase by 90° ($R^r = 0$ and $R^i = 1, -1$).

We now examine special linear polarization states. For $\pm 45^\circ$ linearly polarized light, $\mathcal{P} = 1$, $\chi = 0$, and $\psi = \pi/4, -\pi/4$. Examining Eq. (33), we find, like unpolarized and circularly polarized light, that $\hat{\Phi}_{xx} = \hat{\Phi}_{yy} = S_0/2$. The cross-correlation coefficient takes on the values $R^r = 1, -1$ and $R^i = 0$. To physically produce $\pm 45^\circ$ linearly polarized light, E_x and E_y must have equal powers, must be perfectly correlated, and must be in phase or in antiphase ($R^r = 1, -1$ and $R^i = 0$). The values of $\hat{\Phi}_{xx}$, $\hat{\Phi}_{yy}$, R^r , and R^i are clearly consistent with $\pm 45^\circ$ linear polarization states.

Lastly, we examine horizontally and vertically polarized states. The Poincaré sphere parameters take on the values $\mathcal{P} = 1, \chi = 0$, and

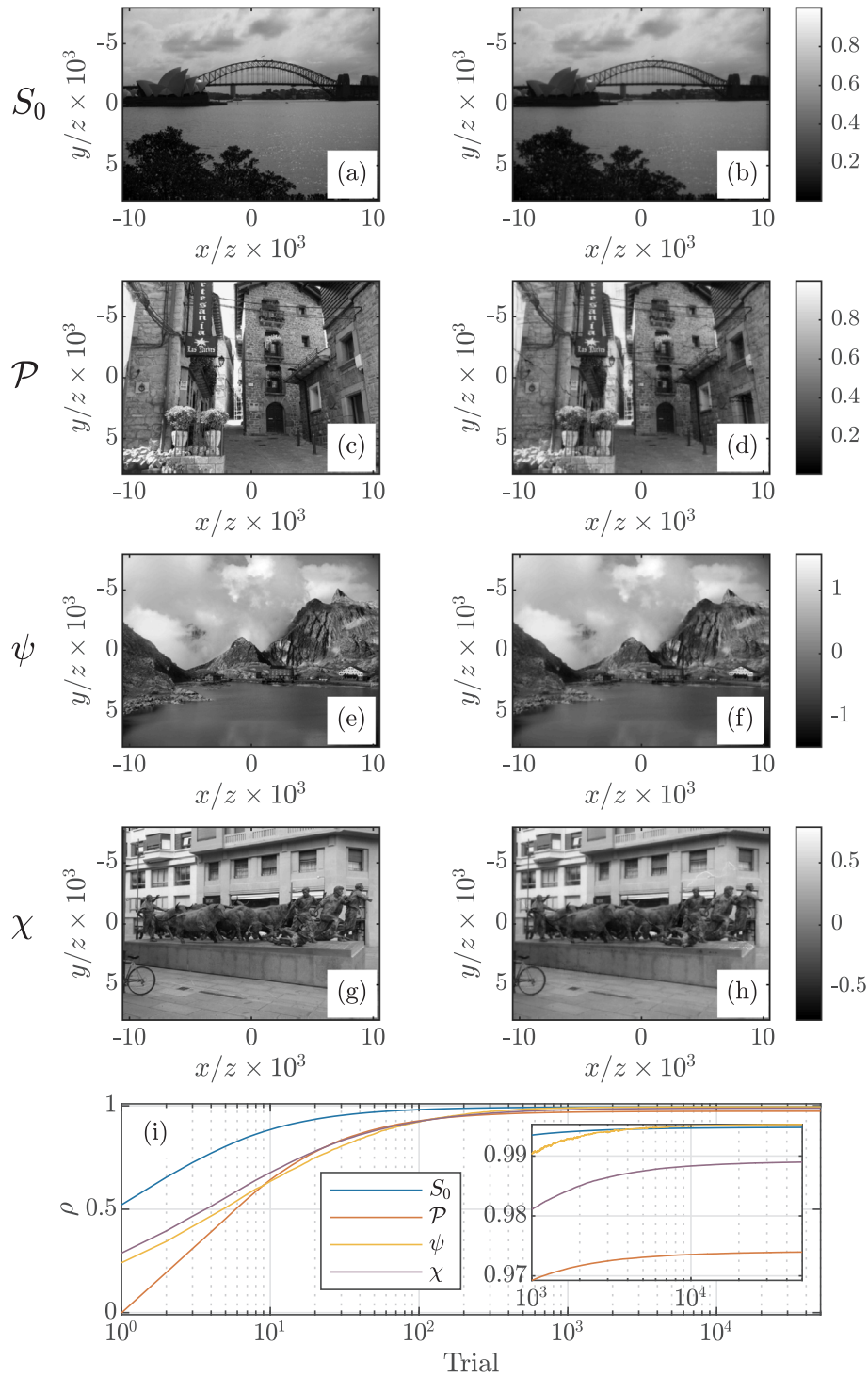


Fig. 4. Theoretical (left column) and simulated (right column) engineered VSMS results—(a) S_0^{thy} , (b) S_0^{sim} , (c) \mathcal{P}^{thy} , (d) \mathcal{P}^{sim} , (e) ψ^{thy} , (f) ψ^{sim} , (g) χ^{thy} , (h) χ^{sim} , and (i) two-dimensional correlation coefficients C of the simulated Poincaré sphere parameters versus trial number. The inset in (i) shows C from trials 1000–50,000.

$\psi = 0, \pi/2$ for horizontally and vertically polarized light, respectively. Substituting these values into Eq. (33) produces $\hat{\Phi}_{xx} = S_0, 0, \hat{\Phi}_{yy} = 0, S_0$, and $R^{r,i}$ is undefined. Like the other polarization states discussed above, these values make physical sense: For horizontally polarized light, all power is in E_x ($\hat{\Phi}_{xx} = S_0$ and $\hat{\Phi}_{yy} = 0$); the opposite is true for vertically polarized light, i.e., all power is in E_y ($\hat{\Phi}_{yy} = S_0$ and $\hat{\Phi}_{xx} = 0$). Since all the field’s power is exclusively in E_x or E_y , the cross-correlation R is irrelevant. This can cause numerical problems using Eq. (33) because $R^{r,i} = 0/0$ is an indeterminate form. To avoid this, we need to check if $\mathcal{P} = 1, \chi = 0$, and $\psi = 0, \pi/2$, and if so, let $R^{r,i}$ be any number in $[-1, 1]$.

Simulation

In this section, we generate an EMGSMS and an engineered VSMS with controllable far-zone S_0, \mathcal{P}, ψ , and χ using the expressions derived in Sections “EMGSMS” and “Engineered VSMS”, respectively. Before presenting and analyzing the results, we briefly discuss the simulation setup.

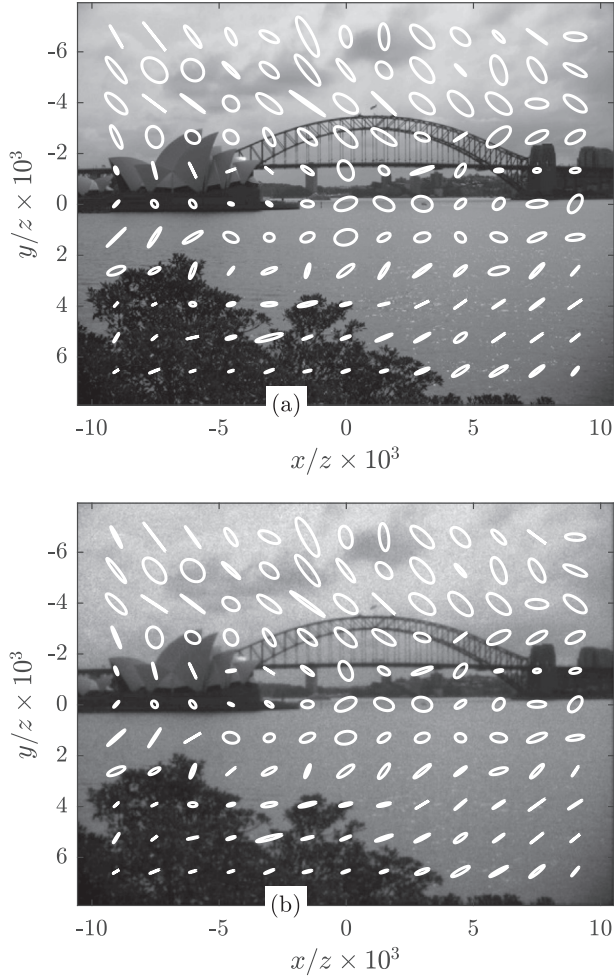


Fig. 5. Polarization ellipses across the beam's profile—(a) theory and (b) simulation (results after 500 trials).

Setup

For these simulations, we used $N_x = N_y = 1024$ grids with a grid spacing $\Delta = 15 \mu\text{m}$. To simulate a Meadowlark Optics Model P512-635 liquid crystal SLM [41], we “windowed” the source plane field in Eq. (3), such that

$$\mathbf{E}(\boldsymbol{\rho}) = \text{rect}\left(\frac{x}{D}\right)\text{rect}\left(\frac{y}{D}\right)[\hat{x}\tau_x(\boldsymbol{\rho})T_x(\boldsymbol{\rho}) + \hat{y}\tau_y(\boldsymbol{\rho})T_y(\boldsymbol{\rho})], \quad (34)$$

where $D = 7.68\text{mm}$, $\text{rect}(x)$ was the rectangle function defined in Ref. [42], and τ_α was

$$\tau_\alpha(\boldsymbol{\rho}) = \begin{cases} C_\alpha \exp\left(-\frac{\rho^2}{4\sigma_\alpha^2}\right) & \text{EMGSMS} \\ 1 & \text{Engineered VSMS} \end{cases} \quad (35)$$

The simulated wavelength was $\lambda = 632.8\text{nm}$.

The complex screens, T_x and T_y , were generated using the procedures described in Sections “EMGSMS” and “Engineered VSMS”. The simulated EMGSMS parameters are given in Table 1. The desired S_0 , \mathcal{P} , ψ , and χ were grayscale images (photographs) shown in Fig. 4(a), (c), (e), and (g), respectively.

We generated 50,000 EMGSMS and engineered VSMS field instances and propagated each to the far zone using FFTs [32,33]. For the EMGSMS, we compared the theoretical far-zone Stokes parameters and $W_{\alpha\beta}(x_1, 0, x_2, 0)$ to the corresponding simulated results. The theoretical far-zone $W_{\alpha\beta}(\boldsymbol{\rho}_1, \boldsymbol{\rho}_2)$ is

$$W_{\alpha\beta}(\boldsymbol{\rho}_1, \boldsymbol{\rho}_2, z) = \frac{\exp\left[\frac{j\pi}{\lambda z}(\rho_1^2 - \rho_2^2)\right] A_{\alpha\beta} B_{\alpha\beta}}{\lambda^2 z^2 C_0} \sum_{m=1}^M \binom{M}{m} \frac{(-1)^{m-1}}{m} \\ \times \frac{\pi^2}{a_{\alpha,\alpha\beta} a_{\beta,\alpha\beta} - b_{\alpha\beta}^2} \exp\left(-\frac{\pi}{2\lambda z^2} \frac{a_{\beta,\alpha\beta} \rho_1^2 - 2b_{\alpha\beta} \boldsymbol{\rho}_1 \cdot \boldsymbol{\rho}_2 + a_{\alpha,\alpha\beta} \rho_2^2}{a_{\alpha,\alpha\beta} a_{\beta,\alpha\beta} - b_{\alpha\beta}^2}\right), \quad (36)$$

where $a_{\alpha,\alpha\beta} = 1/(4\sigma_\alpha^2) + b_{\alpha\beta}$ and $b_{\alpha\beta} = 1/(2m\delta_{\alpha\beta}^2)$ [22]. For the engineered VSMS, we compared the simulated S_0 , \mathcal{P} , ψ , and χ to their desired images.

Results

EMGSMS

Figs. 1 and 2 show the far-zone EMGSMS Stokes parameters and $W_{\alpha\beta}(x_1, 0, x_2, 0)$ results, respectively. In Fig. 1, the left column of images shows the theoretical (superscript “thy” in the figure captions) Stokes parameters; the right column shows the simulated (superscript “sim” in the figure captions) results. The Stokes parameters are organized along the rows— S_0 in row 1 proceeding incrementally to S_3 in row 4. Row headings have been added to aid the reader. The theoretical and simulated Stokes parameters are plotted on the same color scale defined by the color bars at the end of each row. Lastly, row 5 shows the correlation coefficient C , i.e.,

$$C = \frac{\sum_{k=1}^{N_x N_y} (S_i^{\text{sim}}[k] - \bar{S}_i^{\text{sim}})(S_i^{\text{thy}}[k] - \bar{S}_i^{\text{thy}})}{\sqrt{\sum_{k=1}^{N_x N_y} (S_i^{\text{sim}}[k] - \bar{S}_i^{\text{sim}})^2} \sqrt{\sum_{k=1}^{N_x N_y} (S_i^{\text{thy}}[k] - \bar{S}_i^{\text{thy}})^2}}, \quad (37)$$

where $N_x N_y$ is the number of pixels in an image, k is a pixel index, $i = 0, 1, 2, 3$, and \bar{S}_i is the average value of the i^{th} Stokes vector element.

The layout of Fig. 2 mimics the 2×2 CSD matrix \mathbf{W} . Each “element” is labeled for the reader's convenience and composed of a 2×2 group of images. In each group, the theoretical $W_{\alpha\beta}(x_1, 0, x_2, 0)$ are in column 1; the simulated results are in column 2. The real and imaginary parts of $W_{\alpha\beta}(x_1, 0, x_2, 0)$ are in rows 1 and 2, respectively. Both the theoretical and simulated results are plotted on the same false color scale defined by the color bars at rows' end in each group.

The results in Figs. 1 and 2 speak for themselves. Examining Fig. 1(i) shows that the simulated Stokes parameters converge to their theoretical counterparts in roughly 500 trials. To investigate this further, Fig. 3 shows S_0 and the polarization ellipses at several locations across the far-zone beam's profile. The polarization ellipse equations can be found in Ref. [3]. Fig. 3(a) and (b) show the theoretical and simulated results (after 500 trials), respectively. The agreement between Fig. 3(a) and (b) is qualitatively excellent.

Engineered VSMS

Fig. 4 shows the results for the engineered VSMS. The layout of the figure is similar to Fig. 1; however, here, the Poincaré sphere parameters are shown along the rows. Row headings have again been added to aid the reader, and the theoretical, or desired (left column) and simulated (right column) S_0 , \mathcal{P} , ψ , and χ are plotted on the same color scale defined by the color bars at rows' end. Lastly, row 5 reports C [see Eq. (37)] for each of the Poincaré sphere parameters.

Like the EMGSMS results, the agreement between theory and simulation is excellent. Fig. 4(i) shows convergence to the desired Poincaré sphere parameters occurs within approximately 500 trials. Fig. 5 shows the engineered VSMS results corresponding to those in Fig. 3. The results in Figs. 4 and 5 as well as the EMGSMS simulation results validate the electromagnetic Schell-model source synthesis method presented in this paper.

Conclusion

In this paper, we presented a method to produce any physically

realizable electromagnetic Schell-model source by controlling the full CSD matrix \mathbf{W} of the partially coherent beam. In prior works focused on producing electromagnetic Schell-model sources, there was very limited control over the off-diagonal elements of \mathbf{W} , which negatively affected producing VSMSs with S_2 and S_3 Stokes vector components.

We overcame this limitation by using a spatially varying cross-correlation coefficient R between the random numbers that seeded the field's polarization components. We showed both analytically and through examples how a spatially varying R allowed full control over \mathbf{W} . In particular, we generalized the work presented in Refs. [22,28] by demonstrating how to produce any physically realizable EMGSMS and an engineered VSMS that radiated a far-zone beam with customizable Poincaré sphere parameters.

We validated our approach with Monte Carlo simulations, where we produced the two electromagnetic Schell-model sources discussed above, both of which required full \mathbf{W} control. For the EMGSMS, we demonstrated independent control over all EMGSMS parameters. For the engineered VSMS, we demonstrated full control over the far-zone S_0 , ρ , ψ , and χ , which were complex grayscale images. We examined the convergence of the stochastic vector field instances to the theoretical or desired quantities by reporting the correlation coefficients for both sources versus Monte Carlo trial number. We found that both sources converged within 500 field instances. This result will be useful to those who implement our approach for a particular application.

The method we developed in this paper will be useful in SLM-based techniques to synthesize electromagnetic Schell-model sources. Our approach does not require any additional hardware and can be directly implemented on existing setups that produce vector beams [3–5,18,22,43–46]. By expanding the domain of VSMSs that can be generated using existing setups, our work increases the utility of these systems for vector-beam and beam-shaping applications such as free-space optical communications, directed energy, atomic optics, particle manipulation, and optical tweezers.

Appendix A. Supplementary data

Supplementary data associated with this article can be found, in the online version, at <https://doi.org/10.1016/j.rinp.2019.102663>.

References

- [1] Wolf E. Unified theory of coherence and polarization of random electromagnetic beams. *Phys Lett A* 2003;312(5):263–7. [https://doi.org/10.1016/S0375-9601\(03\)00684-4](https://doi.org/10.1016/S0375-9601(03)00684-4).
- [2] Wolf E. *Introduction to the theory of coherence and polarization of light*. Cambridge, UK: Cambridge University; 2007.
- [3] Korotkova O. *Random light beams: theory and applications*. Boca Raton, FL: CRC; 2014.
- [4] Zhan Q, editor. *Vectorial optical fields: fundamentals and applications*. Hackensack, NJ: World Scientific; 2014.
- [5] Cai Y, Chen Y, Yu J, Liu X, Liu L. Generation of partially coherent beams. *Prog Opt* 2017;62:157–223. <https://doi.org/10.1016/bs.po.2016.11.001>.
- [6] Cai Y, Chen Y, Wang F. Generation and propagation of partially coherent beams with nonconventional correlation functions: a review. *J Opt Soc Am A* 2014;31(9):2083–96. <https://doi.org/10.1364/JOSAA.31.002083>.
- [7] Mei Z, Korotkova O, Shchepakina E. Electromagnetic multi-Gaussian Schell-model beams. *J Opt* 2013;15(2). <https://doi.org/10.1088/2040-8978/15/2/025705>.
- [8] Mei Z, Korotkova O. Electromagnetic Schell-model sources generating far fields with stable and flexible concentric rings profiles. *Opt Express* 2016;24(5):5572–83. <https://doi.org/10.1364/OE.24.005572>.
- [9] Mao Y, Wang Y, Mei Z.
- [10] Tong Z, Korotkova O. Electromagnetic nonuniformly correlated beams. *J Opt Soc Am A* 2012;29(10):2154–8. <https://doi.org/10.1364/JOSAA.29.002154>.
- [11] Borghi R, Gori F, Ponomarenko SA. On a class of electromagnetic diffraction-free beams. *J Opt Soc Am A* 2009;26(11):2275–81. <https://doi.org/10.1364/JOSAA.26.002275>.
- [12] Liang C, Mi C, Wang F, Zhao C, Cai Y, Ponomarenko SA. Vector optical coherence lattices generating controllable far-field beam profiles. *Opt Express* 2017;25(9):9872–85. <https://doi.org/10.1364/OE.25.009872>.
- [13] Chen Y, Wang F, Yu J, Liu L, Cai Y. Vector Hermite-Gaussian correlated Schell-model beam. *Opt Express* 2016;24(14):15232–50. <https://doi.org/10.1364/OE.24.015232>.
- [14] Mao H, Chen Y, Liang C, Chen L, Cai Y, Ponomarenko SA. Self-steering partially coherent vector beams. *Opt Express* 2019;27(10):14353–68. <https://doi.org/10.1364/OE.27.014353>.
- [15] Wang F, Wu G, Liu X, Zhu S, Cai Y. Experimental measurement of the beam parameters of an electromagnetic Gaussian Schell-model source. *Opt Lett* 2011;36(14):2722–4. <https://doi.org/10.1364/OL.36.002722>.
- [16] Santarsiero M, Borghi R, Ramírez-Sánchez V. Synthesis of electromagnetic Schell-model sources. *J Opt Soc Am A* 2009;26(6):1437–43. <https://doi.org/10.1364/JOSAA.26.001437>.
- [17] Shirai T, Wolf E. Coherence and polarization of electromagnetic beams modulated by random phase screens and their changes on propagation in free space. *J Opt Soc Am A* 2004;21(10):1907–16. <https://doi.org/10.1364/JOSAA.21.001907>.
- [18] Shirai T, Korotkova O, Wolf E. A method of generating electromagnetic Gaussian Schell-model beams. *J Opt A* 2005;7(5):232–7. <https://doi.org/10.1088/1464-4258/7/5/004>.
- [19] Ostrovsky AS, Martínez-Niconoff G, Arrizón V, Martínez-Vara P, Olvera-Santamaría MA, Rickenstorff-Parrao C. Modulation of coherence and polarization using liquid crystal spatial light modulators. *Opt Express* 2009;17(7):5257–64. <https://doi.org/10.1364/OE.17.005257>.
- [20] Ostrovsky AS, Rodríguez-Zurita G, Meneses-Fabián C, Olvera-Santamaría MA, Rickenstorff-Parrao C. Experimental generating the partially coherent and partially polarized electromagnetic source. *Opt Express* 2010;18(12):12864–71. <https://doi.org/10.1364/OE.18.012864>.
- [21] Ostrovsky AS, Olvera MA, Rickenstorff C, Martínez-Niconoff G, Arrizón V. Generation of a secondary electromagnetic source with desired statistical properties. *Opt Commun* 2010;283(22):4490–3. <https://doi.org/10.1016/j.optcom.2010.04.080>.
- [22] Hyde MW, Bose-Pillai S, Voelz DG, Xiao X. Generation of vector partially coherent optical sources using phase-only spatial light modulators. *Phys Rev Appl* 2016;6. <https://doi.org/10.1103/PhysRevApplied.6.064030>.
- [23] Aarav S, Bhattacharjee A, Wanare H, Jha AK. Efficient generation of propagation-invariant spatially stationary partially coherent fields. *Phys Rev A* 2017;96. <https://doi.org/10.1103/PhysRevA.96.033815>.
- [24] Mishra S, Gautam SK, Naik DN, Chen Z, Pu J, Singh RK.
- [25] Basu S, Hyde MW, Xiao X, Voelz DG, Korotkova O. Computational approaches for generating electromagnetic Gaussian Schell-model sources. *Opt Express* 2014;22(26):31691–707. <https://doi.org/10.1364/OE.22.031691>.
- [26] Gridley MJ, Hyde IV MW, Spencer MF, Basu S. Experimental method of generating electromagnetic Gaussian Schell-model beams. *Proc SPIE* 2015;9617. <https://doi.org/10.1117/12.2192049>.
- [27] Xiao X, Voelz DG, Bose-Pillai SR, Hyde MW. Modeling random screens for pre-defined electromagnetic Gaussian-Schell model sources. *Opt Express* 2017;25(4):3656–65. <https://doi.org/10.1364/OE.25.003656>.
- [28] Hyde MW. Shaping the far-zone intensity, degree of polarization, angle of polarization, and ellipticity angle using vector Schell-model sources. *Results Phys* 2019;12:2242–50. <https://doi.org/10.1016/j.rinp.2019.02.008>.
- [29] Goldstein DH. *Polarized light*. 3rd ed. Boca Raton, FL: CRC; 2011.
- [30] Gori F, Santarsiero M, Borghi R, Ramírez-Sánchez V. Realizability condition for electromagnetic Schell-model sources. *J Opt Soc Am A* 2008;25(5):1016–21. <https://doi.org/10.1364/JOSAA.25.001016>.
- [31] Mandel L, Wolf E. *Optical coherence and quantum optics*. New York, NY: Cambridge University; 1995.
- [32] Schmidt JD. *Numerical simulation of optical wave propagation with examples in MATLAB*. Bellingham, WA: SPIE Press; 2010.
- [33] Voelz DG. *Computational fourier optics: a MATLAB tutorial*. Bellingham, WA: SPIE Press; 2011.
- [34] Yura HT, Hanson SG. Digital simulation of an arbitrary stationary stochastic process by spectral representation. *J Opt Soc Am A* 2011;28(4):675–85. <https://doi.org/10.1364/JOSAA.28.000675>.
- [35] Mack CA. Generating random rough edges, surfaces, and volumes. *Appl. Opt.* 2013;52(7):1472–80. <https://doi.org/10.1364/AO.52.001472>.
- [36] Voelz D, Xiao X, Korotkova O. Numerical modeling of Schell-model beams with arbitrary far-field patterns. *Opt Lett* 2015;40(3):352–5. <https://doi.org/10.1364/OL.40.000352>.
- [37] Goodman JW. *Statistical optics*. 2nd ed. Hoboken, NJ: Wiley; 2015.
- [38] Watkins DS. *Fundamentals of matrix computations*. 2nd ed. New York, NY: Wiley; 2002.
- [39] Roggemann MC, Welsh BM. *Imaging through turbulence*. Boca Raton, FL: CRC; 1996.
- [40] Korotkova O, Hoover BG, Gamiz VL, Wolf E. Coherence and polarization properties of far fields generated by quasi-homogeneous planar electromagnetic sources. *J Opt Soc Am A* 2005;22(11):2547–56. <https://doi.org/10.1364/JOSAA.22.002547>.
- [41] Meadowlark optics spatial light modulator—512 × 512 data sheet; 2018. URL:<http://www.meadowlark.com>.
- [42] Goodman JW. *Introduction to fourier optics*. 3rd ed. Englewood, CO: Roberts & Company; 2005.
- [43] Chen Z, Zeng T, Qian B, Ding J. Complete shaping of optical vector beams. *Opt Express* 2015;23(14):17701–10. <https://doi.org/10.1364/OE.23.017701>.
- [44] Yu Z, Chen H, Chen Z, Hao J, Ding J. Simultaneous tailoring of complete polarization, amplitude and phase of vector beams. *Opt Commun* 2015;345:135–40. <https://doi.org/10.1016/j.optcom.2015.02.008>.
- [45] Rosales-Guzmán C, Bhebbé N, Forbes A. Simultaneous generation of multiple vector beams on a single SLM. *Opt Express* 2017;25(21):25697–706. <https://doi.org/10.1364/OE.25.025697>.
- [46] Rosales-Guzmán C, Ndagano B, Forbes A. A review of complex vector light fields and their applications. *J Opt* 2018;20(12). <https://doi.org/10.1088/2040-8986/aab7d>.